Article:

Full length article

The role of bone metastases on the mechanical competence of human vertebrae

Marco Palanca [a,b,c,*], Giulia Cavazzoni [a,b,c], Enrico Dall'Ara [a,b]

[a] *Dept of Oncology and Metabolism, The University of Sheffield, Sheffield, UK*
[b] *INSIGNEO Institute for In Silico Medicine, The University of Sheffield, Sheffield, UK*
[c] *Dept of Industrial Engineering, Alma Mater Studiorum – University of Bologna, Bologna, Italy*

A R T I C L E   I N F O

A B S T R A C T

Spine is the most common site for bone metastases. The evaluation of the mechanical competence and failure location in metastatic vertebrae is a biomechanical and clinical challenge. Little is known about the failure behaviour of vertebrae with metastatic lesions. The aim of this study was to use combined micro-Computed Tomography (microCT) and time-lapsed mechanical testing to reveal the failure location in metastatic vertebrae.

Fifteen spine segments, each including a metastatic and a radiologically healthy vertebra, were tested in compression up to failure within a microCT. Volumetric strains were measured using Digital Volume Correlation. The images of undeformed and deformed specimens were overlapped to identify the failure location.

Vertebrae with lytic metastases experienced the largest average compressive strains (median $\pm$ standard deviation: -8506 ± 4748 microstrain), followed by the vertebrae with mixed metastases (-7035 ± 15605 microstrain), the radiologically healthy vertebrae (-5743 ± 5697 microstrain), and the vertebrae with blastic metastases (-3150 ± 4641 microstrain). Strain peaks were localised within and nearby the lytic lesions or around the blastic tissue. Failure between the endplate and the metastasis was identified in vertebrae with lytic metastases, whereas failure localised around the metastasis in vertebrae with blastic lesions.

This study showed for the first time the role of metastases on the vertebral internal deformations. While lytic lesions lead to failure of the metastatic vertebra, vertebrae with blastic metastases are more likely to induce failure in the adjacent vertebrae. Nevertheless, every metastatic lesion affects the vertebral deformation differently, making it essential to assess how the lesion affects the bone microstructure. These results suggest that the properties of the lesion (type, size, location within the vertebral body) should be considered when developing clinical tools to predict the risk of fracture in patients with metastatic lesions.

1. Introduction

Longer life expectancy of oncological patients [1] has opened to a new set of challenges for clinicians, physicists and engineers over the last decade, as they aim to provide tools for improving quality of life for these patients. In particular, the management of metastatic diseases (i.e. secondary tumours) is critical. Spine is the most common site for bone metastasis spreading from prostate, breast, lung and kidney primary tumours [2]. The presence of bone metastases degrades the mechanical competence of the vertebrae by affecting their microarchitecture and bone mineral density (BMD) distribution [3]: by reducing bone density (i.e. lytic metastasis), by increasing local BMD and mineralisation (i.e.

blastic metastasis), or by a combination of these features (i.e. mixed metastasis) [4,5]. The bone metastases quickly alter the local bone mechanical properties, and the bone-remodelling process of the surrounding tissues cannot timely compensate for these changes [6,7]. As a consequence, pathologic vertebral fractures are the most frequent complications that affect approximately 30 % of oncological patients with vertebral metastasis [8]. Although there are clinical tools to refer patients with vertebral metastases to orthopaedic consultation (e.g. the Spine Instability Neoplastic Score) [9] and to assess the risk of fracture [10], these tools lack in sensitivity and/or specificity and lead to under- or over-treatment of patients [11,12]. In particular, they partially consider bone mechanical properties, due to the complexity of the

biomechanical problem driven by the heterogenous properties of the vertebrae with lesions.

Several experimental and computational biomechanical studies have analysed the effects of bone metastases on the mechanical behaviour of the vertebrae in order to improve our understanding of their failure location. Digital Image Correlation (DIC) has been used to measure the local strain on the external surface of the vertebrae [13] and Finite Element (FE) models have been used to study the internal deformation of the bone and the stiffness and strength of vertebral body slices [14]. These approaches have shown that type, size and position of the metastasis play a fundamental role in determining the mechanical behaviour (i.e. strain pattern and strain concentration) of metastatic vertebrae. In particular, the type of metastatic tissue (i.e. lytic, blastic or mixed) resulted to be the most relevant parameter to consider for predicting the alteration of the vertebral strength [13].

In fact, even though vertebrae with lytic metastasis showed similar elastic modulus compared to healthy ones, their strength was found to be lower [13–15], and their risk of fracture higher [9,16]. By contrast, vertebrae with blastic metastases were found to have higher strength [15,17] despite their elastic modulus was lower than healthy vertebrae [14].

Size and location of the metastasis within the vertebral body were found to affect the vertebral strength [13,18,19] and experimental strain patterns revealed the potential of considering such features to improve the current clinical supporting system [9].

These studies provide remarkable insight about the overall mechanical properties of metastatic vertebrae, but how the presence of lesions locally contributes to their failure process and failure pattern in realistic loading conditions (e.g. loaded through the intervertebral discs) is still unclear. The complex and heterogeneous microstructure of metastatic vertebrae [17] makes it hard to anticipate their failure location, and to optimise treatments, such as the injection of bone cements where mostly needed [20]. Indeed, contradictory findings are reported in the literature for vertebrae with lytic-like artificial metastasis. Alkalay tested to failure human vertebrae without intervertebral discs under compressive-bending loads and reported a failure process characterized by the collapse of the cortical shell in the proximity of the lytic lesion [21]. Palanca et al. and Rezaei et al. tested three-vertebrae spine segments in similar loading conditions and showed a similar mechanical behaviour [22,23]. Whealan et al., tested three-vertebrae spine segments in compression-flexion and showed different failure mechanisms including vertical compressions, wedge compressions and burst fractures [10]. In all cases, the evaluation of the failure was qualitatively assessed at the end of the test. In addition, Whyne et al. and Tschirhart et al. performed high-speed loading tests on three-vertebrae spine segments and reported an increased risk of burst fracture [24,25]. This evidence highlighted the differences with respect to the typical failure mechanism at the endplate observed in healthy vertebrae subjected to simplified physiological loading [26–29]. Spine segments including vertebrae with blastic metastases are also associated to risk of failure higher than radiologically healthy spine segments, although with a lower fracture incidence than vertebrae with lytic lesions [30].

While it has been showed that metastatic vertebrae (lytic, blastic or mixed) have usually higher risk of fracture compared to radiologically healthy vertebrae, the actual failure mechanism is still unclear. In particular it is still unknown i) if the failure location is close to the lesion, in the cortical shell or close to/involving the vertebral body endplates, ii) if vertebrae with different types of metastases are associated with similar failure location, iii) if the failure happens at the vertebra with lesions or at the adjacent vertebrae. Nevertheless, there are biomechanical challenges in measuring the failure behaviour (i.e. the vertebral failure, the failure location, and the progression of the initial collapse) in vertebrae with metastatic lesions under realistic loading conditions (i.e. loaded through the intervertebral discs). These challenges can be overcome by using a combination of high resolution imaging and mechanical tests. Micro-computed tomography (microCT) imaging of the vertebra

pre- and post-failure and Digital Volume Correlation (DVC) have been used to assess the internal deformation and the onset failure location of different musculoskeletal tissues [31], including healthy vertebrae [26,32]. Nevertheless, this approach has never been used for assessing the mechanical properties and internal deformations in vertebrae with metastatic lesions.

The aim of this study was to evaluate the local internal strain and the failure location in vertebrae with different types of metastases.

2. Materials and methods

2.1. Specimens preparation

The study was approved by the ethical committees of the University of Bologna (n. 17,325, 08/02/2019) and of the University of Sheffield (n. 031782, 22/06/2020). The work was performed in accordance with the Declaration of Helsinki.

Ten-fresh frozen spines from donors with a history of vertebral metastases were obtained from an ethically-approved donation program. The spines were previously prepared as described in [13]. Briefly, the entire spines were scanned with a quantitative computed tomography (qCT; AquilionOne, Toshiba, Japan) with an optimized bone protocol (voltage: 120 kVp, current: 200 mA, slice thickness: 1 mm, in-plane resolution: 0.45 mm) in order to identify the vertebrae with metastasis and the type of metastasis (i.e. lytic, blastic or mixed). The type of metastasis was defined radiologically, based on the identification of focal regions with low density or regions with density much higher than the surrounding trabecular bone.

Fifteen spine segments (Table 1) were dissected, consisting of a metastatic vertebra and an adjacent control vertebra (without any metastatic features visible from the qCT scans) in the middle, and cranial and caudal vertebrae for fixation in the testing rig. Soft tissues around the spine segments were removed without damaging the bone and intervertebral discs. The superior part of the most cranial vertebra and the inferior part of the most caudal vertebra were embedded in polymethylmethacrylate to be mounted in a testing machine. The spine segments were tested in different loading configurations in the elastic regime, as part of a different study [13]. After the mechanical tests, the posterior arches were removed using a hand saw in order to fit a custom jig for in situ mechanical testing within a microCT.

The specimens were kept frozen at $-20\,°C$, thawed for at least 8 h at $4\,°C$ and left at room temperature wrapped in gauzed soaked in saline solution 1 h before the test.

2.2. In situ mechanical tests and microCT imaging

A radiotransparent custom loading device (Fig. 1) [33] was used to axially compress the spine segments inside a microCT (VivaCT80, Scanco Medical Ltd., Switzerland). The device was equipped with a 10 kN load cell (1-C9C/10kN, HBM, Germany) and a 20 mm displacement transducer (WA20, HBM, Germany), which were monitored in real-time during the tests.

Each spine segment was wrapped with gauzes soaked in saline solution to keep the specimen humid during the test. The spine segments were manually loaded through the operating screw using a ratchet wrench, monitoring the applied axial load. The loading protocol [26,32,34] consisted in applying an initial preload of 50 N to firmly hold the specimen within the loading device, ten preconditioning cycles between 0 and 300 N, and stepwise loads up to failure identified as an abrupt drop of the applied load. Generally, failure was obtained in two or three steps: 1) physiological load, defined as the load able to induce peaks in minimum principal strains in the order of $-2500/-3000$ microstrain on the surface of the control vertebra [13]; 2) three times the physiological load; 3) load that induced the failure of one of the vertebral bodies.

After reaching each target load, the loading plate was kept in

Table 1

List of the donors' details, levels included in the spine segments, level of the metastatic vertebra, type of metastasis by evaluation of clinical CT images and microCT images.

ID[a]	Donor	Sex	Age	BMI	Cancer	Segment	Metastatic vertebra	Control vertebra	Metastasis type (qCT)	Metastasis type (uCT)
9	C	F	59	36	Uterine	T10-L1	T11	T12	Lytic	Lytic
10	D	F	51	14	Lung	L1-L4	L2	L3	Lytic	Lytic
11	E	M	75	17	Bladder	T10-L1	T12	T11	Mixed	Mixed
12	F	F	82	22	Breast	T5-T8	T6	T7	Lytic	Lytic
13	F	F	82	22	Breast	T9-T12	T11	T10	Mixed	Mixed
15	F	F	82	22	Breast	L2-L5	L4	L3	Lytic	Lytic
18	G	F	55	17	Breast	T9-T12	T11	T10	Lytic	Mixed
19	G	F	55	17	Breast	T12-L3	L2	L1	Lytic	Blastic
25	K	F	51	41	Breast	T5-T8	T6	T7	Mixed	Mixed
26	K	F	51	41	Breast	T11-L2	T12	L1	Mixed	Mixed
29	L	F	73	24	Lung	T10-L1	T12	T11	Mixed	Blastic
30	L	F	73	24	Lung	L1-L4	L2	L3	Mixed	Blastic
31	M	F	62	57	Adenocarcinoma	T4-T7	T5	T6	Lytic	Lytic
33	O	M	52	17	Prostate	T6-T9	T8	T7	Mixed	Mixed
35	P	M	72	16	Nasopharyngeal	T5-T8	T6	T7	Lytic	Lytic

[a] The same ID used in [13] was used in the present work in order to facilitate the integration of the findings.
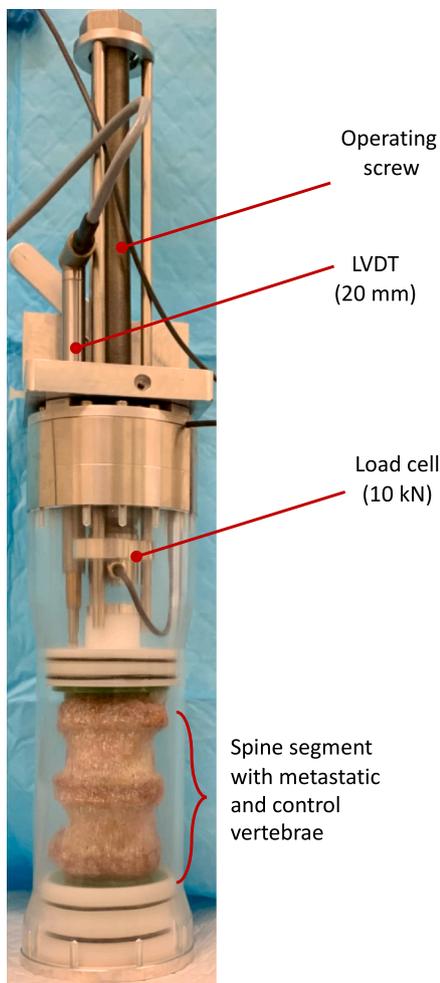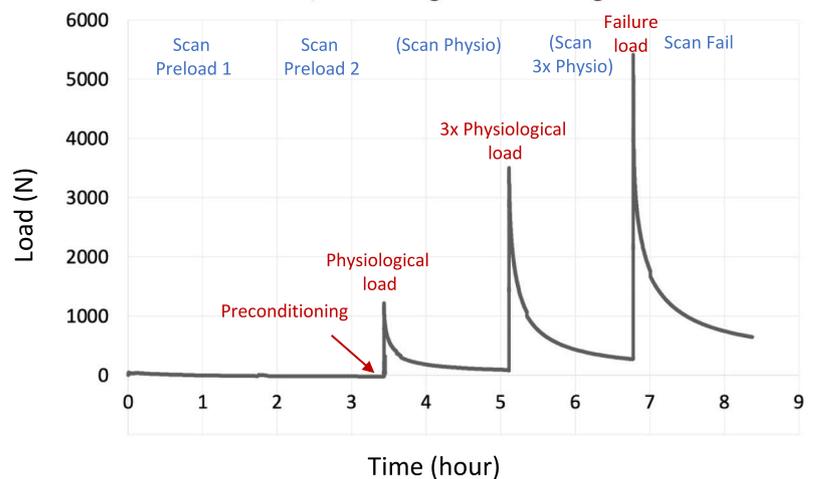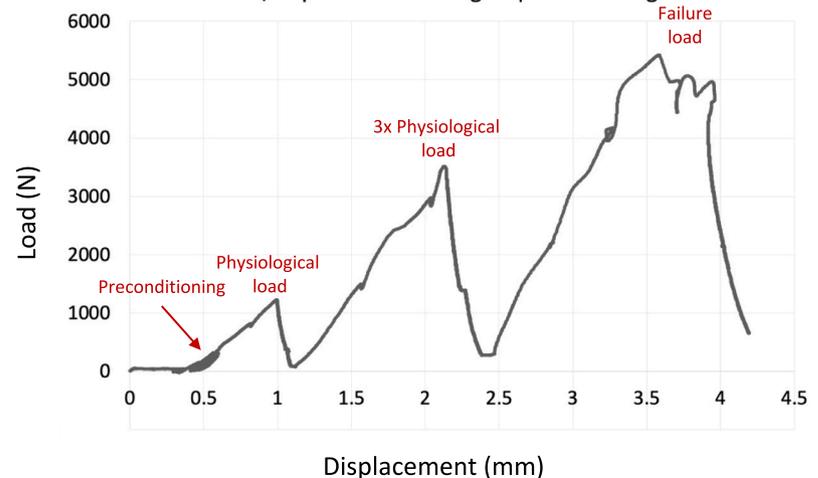
Fig. 1. The custom jig for in situ mechanical tests is displayed on the left. On the top right: example of the load/time curves acquired during one time-lapsed test of a spine segment failed in three steps (only "Scan Preload 1", "Scan Preload 2" and "Scan Fail" have been processed in this study). On the bottom right: the load/displacement curves acquired during the entire test. The duration of the scanning steps (approximately 2 h) is reported in blue boxes, preconditioning and peak loads are indicated in the load/time and load/displacement curves. Definition of the physiological load for each specimen was reported in [13]. (For interpretation of the references to colour in this figure legend, the reader is referred to the web version of this article.)

In some cases, failure occurred at "Scan 3x Physio".

position for 15 min to stabilize the load, and for the duration of the scan immediately thereafter (i.e. during the scan the displacement was kept constant, and the load decreased due to relaxation).

Both metastatic and control vertebral bodies were imaged in the same session using scanning parameters previously optimized for vertebrae [19] (current: 114 mA, voltage: 70kVp, integration time: 300 ms, power: 8 W, isotropic voxel size: 39 μm). Tomograms were reconstructed using the manufacturer software, which includes a polynomial beam hardening correction equation obtained by analysing a wedge phantom with 1200 mg HA/cm^3 density which was found to be more accurate than corrections based on phantoms with lower density [35]. Each specimen was scanned twice in the preloaded condition (later referred to as "Scan Preload 1" and "Scan Preload 2") to evaluate the measurement uncertainty of the Digital Volume Correlation (DVC) approach [36,37]. The microCT scans were used to update the classification of the type of metastases (i.e. lytic, mixed or blastic, Table 1), using the higher image resolution compared to the clinical qCT images. Then, the specimen was scanned after each loading step (approximately 2 h per scan). In this study, only the images obtained in the preload ("Scan Preload 1" and "Scan Preload 2") and failed (later referred to as "Scan Fail") configurations were processed.

2.3. Displacement and strain measurements through digital volume correlation

A global DVC approach (BoneDVC, [38]) was used to evaluate the displacement and strain fields inside the vertebral body. In particular, "Scan Preload 1" and "Scan Preload 2" were used to evaluate the measurement uncertainties of the approach [37], while "Scan Preload 1" and "Scan Fail" were used to measure the strains at failure [32].

Pre-processing of the images was required before the application of the DVC algorithm.

Air bubbles were removed from each image using a custom-made ImageJ [39] script to maintain the contrast between bone and marrow and to avoid measurement errors due to the possible movements of the bubbles between scans. The voxel grey-levels corresponding to the air bubbles were replaced by values similar to those of the bone-marrow.

Rigid body motions, generated by the repositioning of the jig inside the microCT chamber, was reduced by rigid image registration (Amira 6.2, Thermo Fisher Scientific; alignment of principal axes; Lanczos interpolation) between "Scan Preload 1" and "Scan Preload 2" and between "Scan Preload 1" and "Scan Fail".

Binary masks (value equal to "0" for background and equal to "1" for bone) were created in ImageJ [39] to exclude features outside the vertebral body that may affect DVC assessment (e.g. costovertebral joints, wet gauzes). To create the mask, for each scan a Gaussian 3D filter (sigma = 5, i.e. standard deviation of the Gaussian) was applied to reduce the high frequency noise, then a manual selection of the single-level threshold was performed. Space among trabeculae (inside the vertebra) was filled using filling algorithms. A mask for the evaluation of the measurement uncertainty was created by merging the masks of "Scan Preload 1" and "Scan2". A mask for the strain measurement at failure was created by merging the masks of "Scan Preload 1" and "Scan Fail".

Operating principles of BoneDVC are widely described elsewhere [36,38]. Briefly, two images (i.e. "Scan Preload 1" and "Scan Preload 2", or "Scan Preload 1" and "Scan Fail") were elastically registered (Sheffield Image Registration Toolkit, ShIRT) to compute the displacement field required to transform the undeformed image ("Scan Preload 1") into the deformed one ("Scan Preload 2" or "Scan Fail"). The registration algorithm consists in superimposing on the images a regular parallelepiped grid with cubic cells with side length equal to the nodal spacing (NS). ShIRT solves the registration equations at the nodes of the grid [40,41] within the binary mask. The registration equations include the displacement terms and a term to account for potential changes in the grey levels. Trilinear interpolation is assumed within the cells of the

grid. The registration is solved by adding a smoothing coefficient in the displacement field to overcome the poorly conditioned problem. The problem is then solved iteratively to compensate for large displacements. The strain field is obtained differentiating the displacement field with an FE software package (Mechanical APDL v19, ANSYS, USA). To do so, a linear hexahedral mesh equal to the hexahedral DVC grid was imported in the FE software. The displacement calculated from the elastic registration in each node of the grid were imposed at the nodes of the FE elements and then differentiated into strains. The FE software package was used only to differentiate the displacements into strain and to visualize the results in the considered volume of interest.

2.4. Identification of the failure location

In order to visualize the bone microstructure before and after the failure, "Scan Preload 1" and "Scan Fail" were aligned. "Scan Fail" was rigidly co-registered in space (Amira 6.2.0, Thermo Fisher Scientific, USA) to "Scan Preload 1", performing alignment of principal axes and Lanczos interpolation. The co-registered images were then binarized using the Max Entropy thresholding algorithm [42] in ImageJ [39] and overlapped in different colours (red: preload condition, green: failure condition, yellow: overlapped conditions) to highlight the failure location in the control or metastatic vertebrae.

2.5. Evaluation metrics

"Scan Preload 1" images were used to evaluate the bone volume fraction (BV/TV), the volume of the vertebral body, and the average cross-section area of the vertebral body. A 3D median filter (sigma equal to 0.5, 0.5, 0.5) was applied to reduce the high frequency noise of the microCT images without compromising the contrast between bone and marrow [43,44]. A single level threshold, calculated as the value identified by the Otsu Thresholding algorithm (ImageJ, National Institute of Health, USA) increased by 5 %, was applied to the images. The BV/TV over the entire vertebra was evaluated as the ratio between the volume of the bone (regardless of metastatic and healthy tissues) and the volume of the entire vertebra (CTAn, Brucker). The average cross-section area was computed as the ratio between the volume and the height of the vertebral body. The volumetric Bone Mineral Density (vBMD) was calculated using the calibration equation proposed in [45].

Volumes of the metastatic lesion were calculated through a manual segmentation of the CT scan and reported as percentage of the volume of the vertebral body [13].

The load associated with the initiation of the failure (failure load) was defined as the peak load in the last loading step (before a sudden drop of the load). Apparent failure stress for each failed vertebra was calculated as the ratio between the failure load of the spine segment and the average cross-section area of the failed vertebra.

DVC measurement spatial resolution equal to 1.95 mm (NS = 50) was selected as the smallest size that still produced acceptable errors (below 1000 microstrain) for this application [46]. Thus, strain measurement uncertainty of the DVC was quantified in terms of mean absolute error (MAER) and standard deviation of the error (SDER) [37] for each considered vertebra.

Principal strains were calculated for the nodes of the DVC grid within the vertebral body for the loading step at failure. Average and standard deviation of the maximum and minimum principal strains were measured for each metastatic or control vertebra. Medians of the averaged principal strains (minimum or maximum) were computed for the different groups of vertebrae (lytic, blastic, mixed, control).

For each segment, the percentage strain difference [13] was defined as:

$$\text{Strain Difference }(\%) = \frac{\overline{\varepsilon}\text{ (metastatic vertebra)} - \overline{\varepsilon}\text{ (control vertebra)}}{\overline{\varepsilon}\text{ (control vertebra)}} \times 100$$

where $\bar{\varepsilon}$ (*metastatic vertebra*) represents the average strain within the metastatic vertebra and $\bar{\varepsilon}$ (*control vertebra*) the average strain inside the control vertebra. For both maximum and minimum principal strain, percentage strain difference was evaluated.

2.6. Statistics

The Kruskal-Wallis test followed by a post hoc (uncorrected Dunn's test) was used to assess if significant difference existed in the BV/TV, the failure load, the apparent failure stress or the principal strains measured among vertebrae with different types of metastases and control vertebrae.

Linear correlations between the minimum principal strain and the size of the lesion, the failure load, or the apparent failure stress were explored for the different types of metastatic vertebrae.

3. Results

3.1. Density and mechanical properties

For all cases, the BV/TV and vBMD values of the control vertebrae were in the range of healthy bone [47,48]. The lesion type significantly affected the BV/TV within the vertebral body (Kruskal-Wallis; *p*-value = 0.02). In particular, the BV/TV of vertebrae with lytic metastases was 55

% lower than the BV/TV of vertebrae with mixed metastasis (p-value = 0.03) and 77 % lower than the BV/TV of vertebrae with blastic metastasis (p-value = 0.01). The BV/TV of vertebrae with blastic metastasis was 246 % higher than the BV/TV of control vertebrae (p-value = 0.03) (Fig. 2).

The failure loads and the apparent failure stresses are reported for each vertebra (Table 2 and Fig. 2). The control vertebrae showed an apparent failure stress of 2.0 ± 2.2 MPa. Higher values of apparent failure stress were found for spine segments with mixed metastases (2.3 ± 2.5 MPa), followed by segments with lytic metastases (2.8 ± 1.6 MPa) and segments with blastic metastases (4.2 MPa). However, these differences were not significant (Kruskal-Wallis; failure load: p-value = 0.64, apparent failure stress: p-value = 0.75).

3.2. Strains

Reasonable DVC strain measurement uncertainties were found for metastatic (MAER range: 242 to 870 microstrain; SDER range: 254 to 689 microstrain) and control (MAER range: 263 to 1356 microstrain; SDER range: 312 to 599 microstrain) vertebrae.

The maximum principal strains (Eps1, Kruskal-Wallis, p-value = 0.35) or minimum principal strains (Eps3, Kruskal-Wallis, p-value = 0.41) were not significantly affected by the type of lesions (lytic, blastic, mixed, control). However, vertebrae with lytic metastasis were associated with largest absolute value of the maximum principal strain
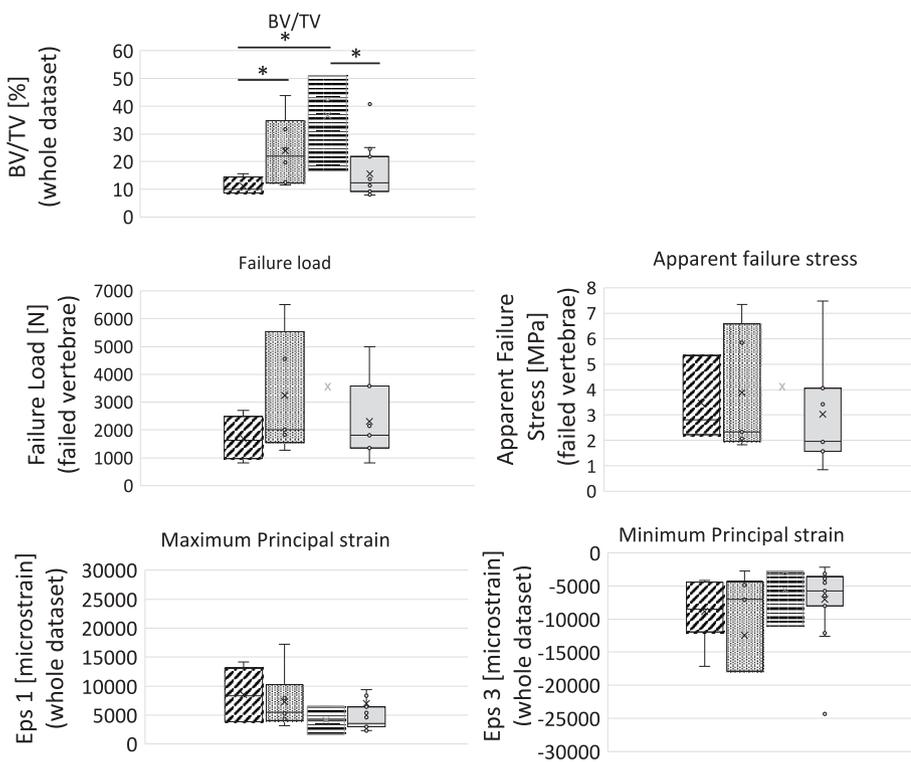
Fig. 2. Box plots for the bone volume fraction (BV/TV), failure load, apparent failure stress maximum principal strain (Eps 1), and minimum principal strain (Eps 3) for the different types of vertebrae: vertebrae with lytic metastasis (box plots with oblique stripes), mixed metastasis (dotted box plots), blastic metastasis (box plots with horizontal stripes) and control vertebrae (filled box plots).

The orange circles on the cross sections indicate the region with the metastasis.
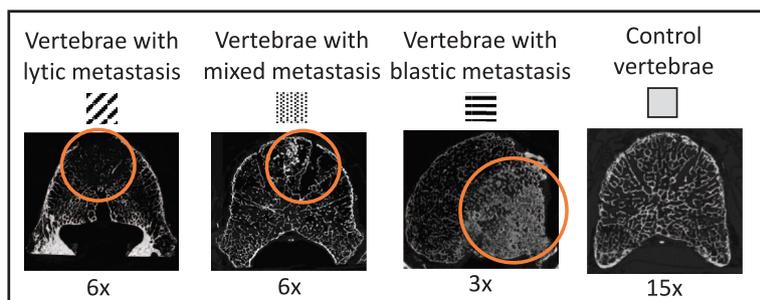
Table 2
List of the spine segments with indication of the failed vertebra, failure location, total volume, mean cross-section area, apparent failure stress (only for failed vertebrae), and lesion size. In the failure location column, sup ep: close to/involving the superior endplate, inf ep: close to/involving the inferior endplate, both ep: close to/involving the superior and inferior endplates.

ID[a]	Segment	Vertebrae	Type of vertebra and metastasis	Failed vertebra	Failure location	Failure load [N]	BV/TV [%]	Estimated vBMD [mg/ml]	Total Volume [mm^3]	Average cross-section area [mm^2]	Apparent failure stress [MPa]	Lesion size [VB% (cm^3)]
9	T9-L1	T11	Lytic	N	–	–	8.43	89	24,459	832	–	2 (0.4)
		T12	Control	Y	Sup ep	1800	7.95	84	28,090	916	2.0	–
10	L1-L4	L2	Lytic	Y	Inf ep	807	8.66	92	18,473	643	1.2	36 (10.1)
		L3	Control	Y	Sup ep	807	7.99	85	28,563	956	0.8	–
12	T5-T8	T6	Lytic	Y	Inf ep	1450	9.50	101	11,313	514	2.8	5 (0.6)
		T7	Control	N	–	–	11.30	121	13,359	544	–	–
15	L1-L5	L4	Lytic	Y	Inf ep	1800	10.32	110	26,191	807	2.2	20 (5.2)
		L3	Control	N	–	–	11.46	123	26,842	887	–	–
31	T4-T7	T5	Lytic	Y	Sup ep	2705	15.56	169	11,482	506	5.3	6 (0.8)
		T6	Control	N	–	–	13.65	147	14,692	569	–	–
35	T4-T8	T6	Lytic	N	–	–	14.14	153	10,454	405	–	10 (1.0)
		T7	Control	Y	Sup ep	1350	14.54	157	10,187	394	3.4	–
11	T10-L1	T12	Mixed	Y	Sup ep	1998	12.54	135	34,847	1087	1.8	4 (1.4)
		T11	Control	N	–	–	9.96	106	32,909	954	–	–
13	T9-T12	T11	Mixed	Y	Sup ep	1273	11.63	125	19,713	613	2.1	12 (2.2)
		T10	Control	N	–	–	12.25	132	17,215	569	–	–
18	T9-T12	T11	Mixed	Y	Both ep	1834	19.57	213	18,443	783	2.3	20 (5.0)
		T10	Control	N	–	–	14.28	154	19,295	667	–	–
25	T5-T8	T6	Mixed	N	–	–	31.70	348	13,192	577	–	31 (4.3)
		T7	Control	Y	Sup ep	5000	25.12	275	14,917	668	7.5	–
26	T11-L2	T12	Mixed	Y	Sup ep	6510	24.50	268	28,219	886	7.3	19 (5.3)
		L1	Control	N	–	–	24.54	268	32,409	975	–	–
33	T6-T9	T7	Mixed	Y	Both ep	4563	43.78	482	21,015	781	5.8	47 (10.0)
		T8	Control	N	–	–	40.83	449	21,461	797	–	–
19	T12-L3	L2	Blastic	Y	Sup ep	3579	42.41	467	21,886	853	4.2	34 (7.5)
		L1	Control	Y	Sup ep	3579	21.70	237	26,747	883	4.05	–
29	T10-L1	T12	Blastic	N	–	–	16.63	181	29,978	1014	–	12 (3.6)
		T11	Control	Y	Both ep	1444	9.26	99	26,129	913	1.6	–
30	L1-L4	L2	Blastic	N	–	–	50.96	562	36,660	1163	–	27 (9.9)
		L3	Control	Y	Sup ep	2152	9.14	97	38,075	1107	2.0	–

[a] The same ID used in [13] was used in the present work in order to facilitate the integration of the results.
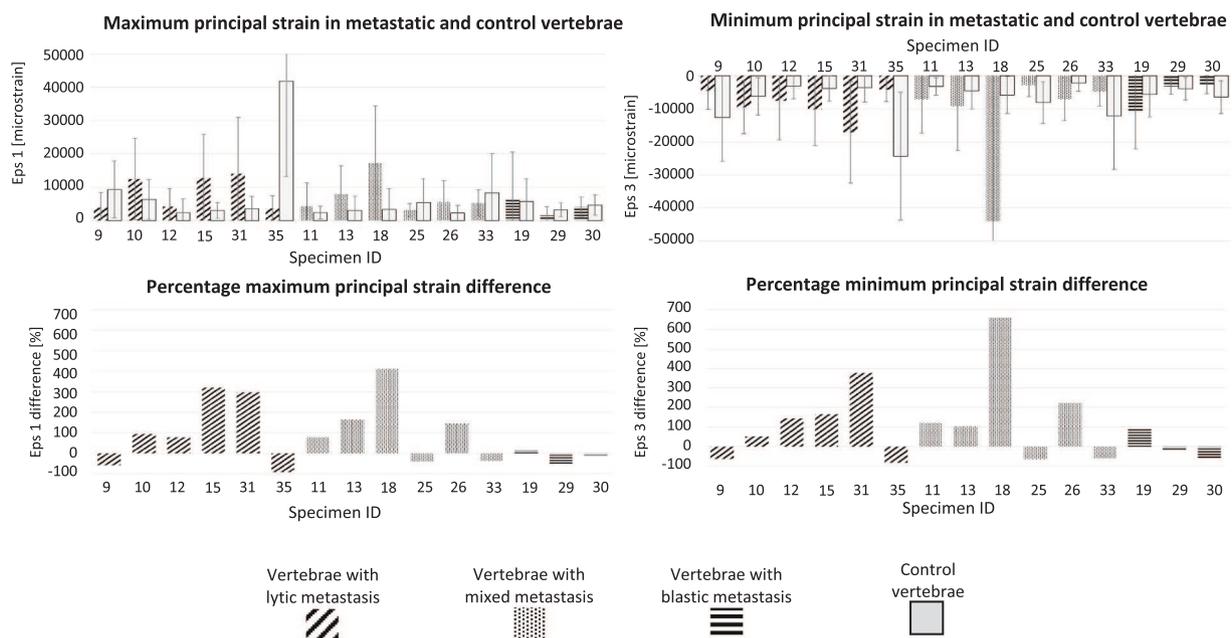

Fig. 3. Top: Median maximum (Eps 1) and minimum (Eps 3) principal strains in vertebrae with lytic metastases, mixed metastases, blastic metastases, and control adjacent vertebrae: the average and standard deviation over each vertebral body is plotted. Bottom: Percentage differences for the maximum and minimum principal strain in spine segments with lytic, mixed, and blastic metastases.

No significant correlations ($p > 0.05$) were observed between the average Eps3 at failure evaluated in the metastatic vertebrae and the size of the lesions (for data from the different types of metastases or for pooled data), the failure load or the apparent failure stress.

(median ± standard deviation: 8357 ± 5077 microstrain), followed by vertebrae with mixed metastasis (5500 ± 5125 microstrain), vertebrae with blastic metastasis (4170 ± 2447 microstrain) and control vertebrae (3560 ± 9873 microstrain) (Fig. 2, Fig. 3 and Supplementary Material). Similarly, largest minimum principal strains were observed in the vertebrae with lytic metastases (median ± standard deviation: −8506

± 4748 microstrain), followed by the vertebrae with mixed metastasis (−7035 ± 15605 microstrain), the control vertebrae (−5743 ± 5697 microstrain), and the vertebrae with blastic metastasis (−3153 ± 4641 microstrain) (Figs. 2, 3 and Supplementary Material).

Vertebrae with metastases were subjected to larger deformations
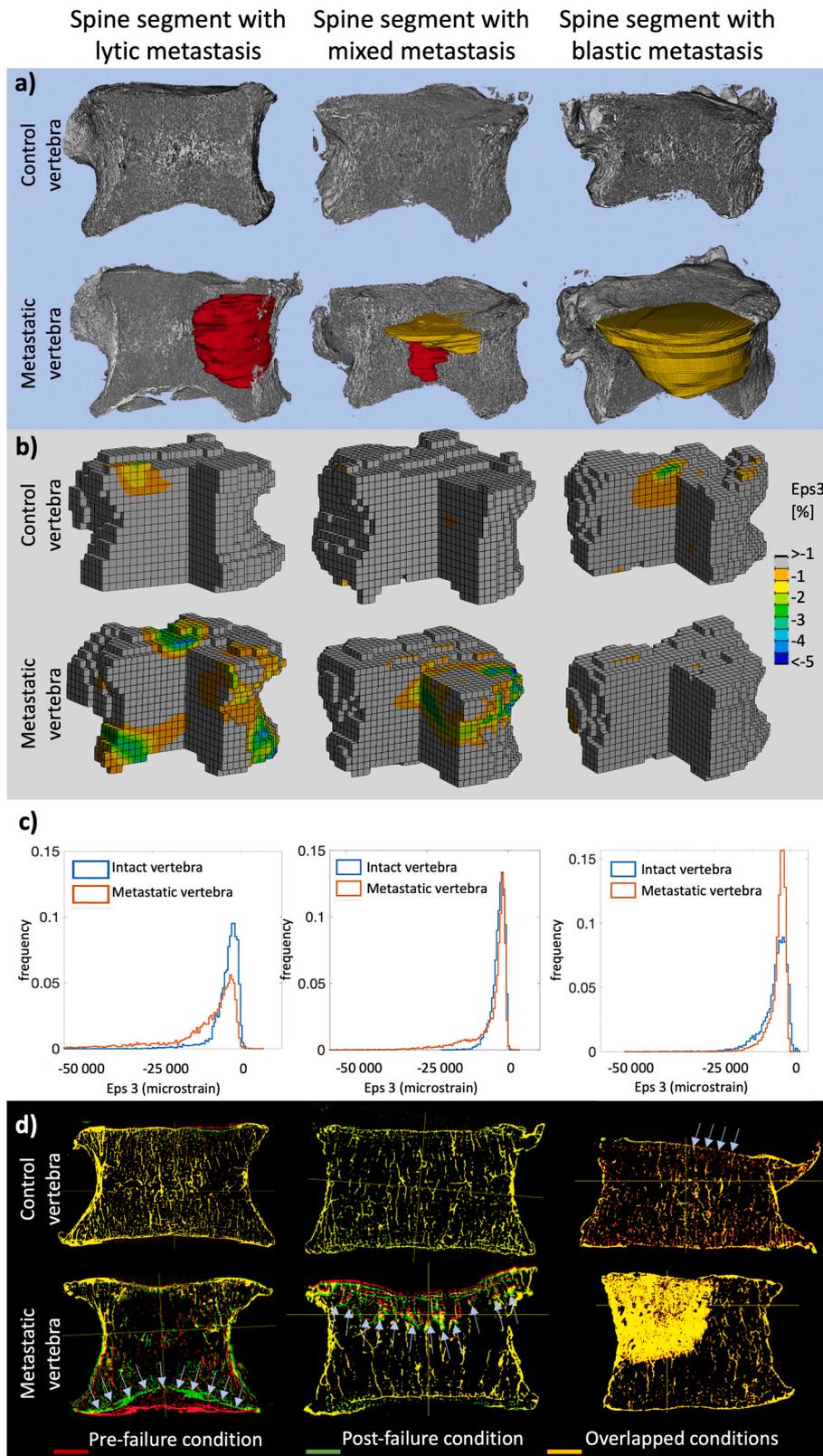
Fig. 4. Examples of spine segments with lytic metastasis (left column), mixed metastasis (central column), or blastic metastasis (right column). Each spine segment consists in a control and a metastatic vertebra.

a) 3D shape of the vertebrae and internal trabecular pattern. The lytic and blastic metastatic tissue are reported in red and yellow, respectively. b) Minimum principal strains lower than −10,000 microstrain are reported. c) Frequency plots of the minimum principal strain are reported for each spine segment, splitting between the metastatic (orange) and the control (blue) vertebrae. d) MicroCT scans of the vertebrae before (red) and after (green) failure are overlapped in order to highlight the failure location (light blue arrows). Regions that overlap in the two images are reported in yellow. (For interpretation of the references to colour in this figure legend, the reader is referred to the web version of this article.)

than control vertebrae in case of mixed (112 % median percentage maximum principal strain difference and 112 % percentage minimum principal strain difference) and lytic (86 % percentage maximum principal strain difference and 99 % percentage minimum principal strain difference) metastasis. Conversely, vertebrae with blastic metastasis were less deformed than control vertebrae and showed a percentage maximum principal strain difference of −10 % and a percentage minimum principal strain difference of −19 % (Fig. 3).

Frequency plots of the minimum principal strains showed higher strains in the vertebrae with lytic metastases, which were confirmed by a larger region of tissue deformed beyond the bone failure strain (≈ −10,000 microstrain) compared to the corresponding control vertebra (Fig. 4). In particular, the high strains localised mainly in the region within or close to the lytic tissue. Conversely, in spine segments with blastic metastases, higher deformations were found in regions of the control vertebra. The vertebrae with mixed metastasis showed a combination of the behaviours observed in the vertebrae with lytic or blastic lesions (Fig. 4).

3.3. Failure location

The failure patterns obtained in this study were comparable with the failure patterns found clinically (i.e. vertebral compression failure) [49–51] as well as in biomechanical studies performed in similar loading conditions [26,29]. Failure of the metastatic vertebra occurred in 67 % of the cases of segments with lytic metastases, in 67 % of cases with mixed metastases, and 33 % of cases with blastic metastases. The onset failure localised at the endplates or in the tissue close to the endplates of the vertebrae (Fig. 4 and Supplementary Material), in particular in 70 % of the cases, the tissue close to or involving the superior endplate failed (Table 2). In vertebrae with lytic metastases the collapse usually occurred in the tissue between the endplate and the metastatic lesions. In cases of vertebrae with small lytic metastases (i.e. lesions size <20 % of the vertebral body), the failure was localised close to the endplates (Fig. 5). In the case of large lytic metastases, the endplate failed in compression or bending (before or after the failure of the tissue close to it) and there was involvement of the cortical shell (Fig. 5). A different

failure location, consisting in the collapse of the healthy tissue around the metastatic lesion, was observed for the only vertebra with blastic metastasis that failed (Fig. 5). In this case, the regions within the blastic tissue experienced lower strain compared to the failed surrounding tissue. Vertebrae with mixed metastases showed different failure location, including the behaviours observed for vertebrae with lytic or blastic metastases.

When the control vertebrae failed first, the failure location was on the same or opposite side compared to the location of the metastatic lesion in the adjacent vertebra. In case of blastic metastasis, the larger deformation on the endplate and the tissue close to the endplate of the adjacent control vertebra were usually axially aligned with the position of the blastic metastasis. Conversely, in case of lytic metastases, the largest deformation in the control vertebra was opposite to the position of the lytic lesion in the metastatic vertebra (Fig. 6).

4. Discussion

The aim of the study was to evaluate the local internal strain and the failure location of vertebrae with different types of metastases. Fifteen spine segments containing a control vertebra and a metastatic vertebra were tested using state of the art microCT imaging and DVC biomechanical assessment, that enabled, for the first time, the measurement of the internal deformation of the vertebral body with lesions and to identify the failure location.

The control vertebrae showed values of BV/TV and vBMD [45] within typical ranges of subjects without osteoporosis (>80 mg/cc) [47,48]. Conversely, the metastatic vertebrae showed a wide range of BV/TV, which reflects the high variability of local bone mineral density affected by the metastatic lesions.

Tests were designed to transmit the same load through the vertebral bodies of the spine segment through the intervertebral discs and vertebral endplates [52], so that both metastatic and control vertebral bodies experienced a similar axial load. This approach enabled the simultaneous evaluation of the behaviour of two adjacent vertebrae with similar anatomy and size. As a result, the deformation measured in the vertebral bodies of the metastatic vertebrae could be normalised with respect
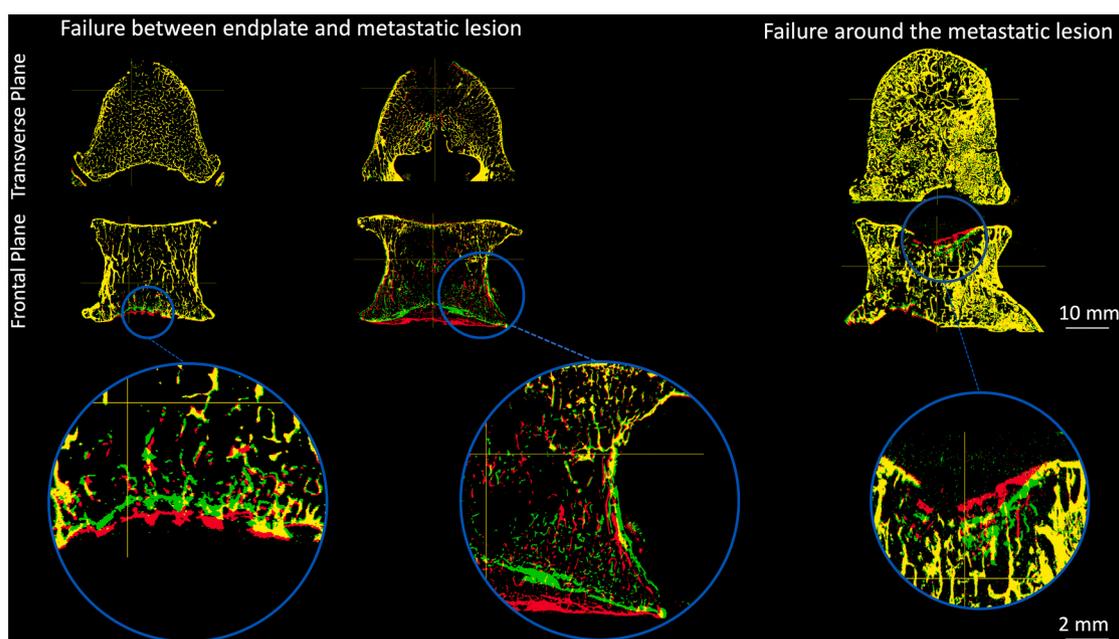

Fig. 5. Microstructural deformation of the bone tissue for representative cases where different failure features were observed. Unloaded condition in red colour, failed condition in green colour, overlap in yellow colour. Examples of different failures: failure of the tissue close to the endplate and of the endplate (left, for lytic lesion; right, for mixed lesion) or failure of the endplate and its surrounding tissue with cortical shell involvement (centre, for lytic lesion). (For interpretation of the references to colour in this figure legend, the reader is referred to the web version of this article.)
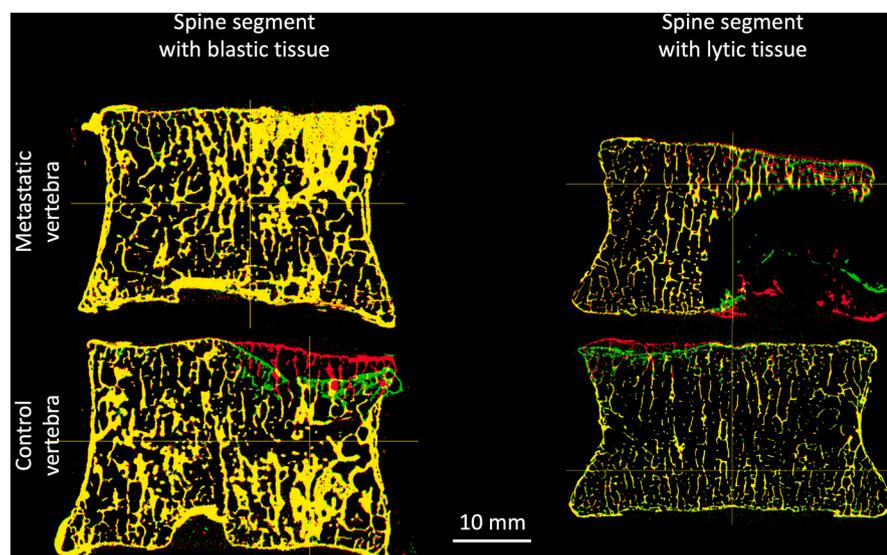
Fig. 6. Failure of control vertebra: in case of vertebrae with blastic tissue, the failure region of the control vertebra was usually axially aligned with the position of the blastic tissue. In case of vertebrae with lytic tissue, the failure region of the control vertebra was usually opposite to the position of the lytic lesion. Unloaded condition in red colour, failed condition in green colour, overlap in yellow colour. (For interpretation of the references to colour in this figure legend, the reader is referred to the web version of this article.)

those of the healthy (control) vertebrae [13], understanding the effect of the metastases.

The strain analysis on the spine segments showed that in most cases the vertebrae with lytic or mixed metastases were subjected to higher deformations than the corresponding control vertebrae and in most cases failed before the adjacent healthy ones. In particular, in case of vertebrae with lytic lesions the strain concentrations were located in the tissue affected by the lytic lesion [32], or in regions with low BMD near the lesion [3,53]. By contrast, the blastic tissue did not experience large deformation, and the surrounding regions, subjected to larger deformations, failed [3]. These findings can be explained by the fact that lytic tissue is less dense and less stiff than healthy trabecular bone and that blastic tissue is denser and stiffer than healthy trabecular bone [3]. The local strains in vertebrae with mixed metastasis cannot be generalized since they reflected the presence of the lytic and blastic tissue inside the same vertebral body.

Nevertheless, it should be noted that every lesion affected the deformation of the bone tissue in a different way, making it essential to assess in detail the properties of the lesion (i.e. type, size, position, shape), of the bone microstructure and of the local deformation of the tissues, in order to identify the failure behaviour of the spine segment. For example, while in most cases the vertebra with the metastatic lesions failed, in two spine segments with lytic metastasis (i.e. ID9 and ID35) the control vertebra did fail. In the first case (ID9), this atypical behaviour could be explained by the presence of an osteophyte that connected the two vertebrae. Despite the mechanical role played by the osteophytes is still unclear, they can change the load transmission between vertebrae and perturb the strain pattern in the nearby tissue [54]. In the second case (ID35), despite the presence of a lytic lesion, the vertebra was "protected" by an unusual thick cortical shell, which probably bore most of the transmitted load. For this subject the clinical record reported a treatment with vitamin D which is known to affect the bone remodelling and may have affected the microstructure and material properties of the bone tissue. One spine segment (ID18) with mixed metastasis showed unusually large deformation. A detailed analysis of the microCT scan highlighted that the lytic lesion affected the cortical shell, explaining the large deformation.

Depending on the bone microstructure close to the endplates, different failure locations were observed. Lytic lesions replace the bone mineralised tissue with soft tissue containing mainly bone marrow and cancer cells [4,55]. Therefore, in most cases the low BV/TV trabecular bone tissue close to the endplate collapses since the lytic tissue has poor mechanical competence and only partially supports the applied load

[56]. In this study, these mechanisms could be identified experimentally. A similar failure behaviour was described in healthy and osteoporotic vertebrae loaded in axial compression through the intervertebral discs [26,57]. This comparison suggests that in cases where the lytic lesions are localised close to the endplate, the metastatic vertebrae are subjected to failure location similar to those of vertebrae with low BMD [56]. In other studies where vertebrae with artificial metastasis were tested, they showed different failure mechanisms, with involvement of the cortical shell [21,22]. The different failure mechanisms observed in this and those studies are probably due to the different loading conditions the vertebral body was subjected to (through the intervertebral disc at the endplates in this study and through rigid plates after removing the endplates in the other study [22]), in metastatic lesions (real metastasis which localise inside the vertebral body in this study vs simplified lesions induced from the external portion of the vertebral body in the other studies), and the assessment of the deformation (evaluation of the inner microstructure and volumetric strain field in this study vs standard apparent or superficial measurement in the other studies). Moreover, our approach enabled the observation of another failure behaviour: in vertebrae with large lytic lesions (i.e. larger than 20 % of the volume of the vertebral body) the cortical shell was deformed radially towards the outside of the vertebral body, similar to what would happen in a burst fracture of vertebrae with lytic-like metastasis axially loaded at high rate [24,58]. In most cases the mechanical tests identified failure locations that are typically observed in cases associated with backpain, kyphosis or neurologic impairment [51]. To the best authors' knowledge, these initial failure locations have never been observed in vertebrae with artificially induced lytic lesions [22,23] or in mechanical tests that used animal spine segments [32]. In fact, this study highlights the importance of performing these complex in situ biomechanical tests on human spine segments, monitoring what happens at the internal and external portions of the vertebral bodies.

Blastic metastases led to two different failure scenarios: failure of the metastatic vertebra or failure of the adjacent vertebra. In the first case, the trabecular pattern of the vertebra, which is optimized to bear the physiological loads [59,60], is affected by the presence of the dense material. Therefore, the healthy bone tissue surrounding the blastic tissue is probably subjected to unusually high stresses they are not optimized for, leading to fracture. For example, in this study one vertebra with blastic tissue inside a mixed metastasis (ID33, Fig. 5) showed a localised failure location of the superior endplate, with a hinge close to the blastic lesion, which probably creates an unbalance of the stiffness of the tissue underneath the endplate. A similar scenario was

observed in case of augmented vertebral bodies, from porcine vertebrae, when the bone cement did not connect the two endplates [61]. In other cases, the presence of blastic metastases that involve the endplate can trigger the failure of the adjacent (radiologically healthy) vertebra (Fig. 6). In this case the load transmitted by the intervertebral discs is altered by the high-BMD region, and the adjacent vertebra is overloaded. Similar event was also observed in human spine segments with augmented vertebrae, where the adjacent (not treated) vertebra failed [62].

The identified location of the failure in vertebrae with metastases close to the endplate remarks the importance of testing the vertebral bodies through the IVDs, and paves the way to future clinical tools for the identification of which lesions reduce the bone strength and need treatments. The high variability in the failure of the metastatic vertebrae highlights the importance of developing patient-specific tools able to consider how the features of the metastasis affect the biomechanical properties of the vertebrae. Indeed, this data can be used to inform and update clinical scoring systems (e.g. SINS [9]), suggesting that including biomechanical and morphological characteristics of the lesions is required to identify patients at high risk of fracture. Moreover, this unique dataset of experimental measurements of internal deformation can be used to validate the outputs of computational biomechanical models that aim to predict the risk of fracture of metastatic vertebrae [63] validating not only the apparent mechanical properties (i.e. stiffness and strength) but also the internal deformation and damage localization.

This study has some limitations. First, the posterior arches of the vertebrae were removed in order to fit the jig in the microCT scanner. Despite this anatomical change modifies the biomechanics of the spine segment, removing the mechanical contribution of the posterior element and of the facet joints [64], it allows loading the vertebral bodies under compression through the IVDs, which is the dominant load component they are subjected to [65]. Moreover, the vertebral body has a predominant importance since the vertebral body compression fracture is the most common fragility reported in the literature [66]. While this approach cannot be used to study the effect of lesions affecting the posterior elements on the vertebral strength, it can be adapted in the future to test larger regions of interest in microCT with larger scanning volume. Second, only one loading condition (i.e. axial compression applied to the spine segment) was studied. While other loading scenarios would help in elucidating the failure location of metastatic vertebrae, only one loading condition can be used to evaluate the post failure properties of the spine segments. In the future, this approach could be extended to other combined loading (for example flexion and extension ± torsion) which causes severe spine instability and neurologic impairments, by re-designing the loading jig and using a microCT scanner with larger scanning chamber. Third, the slow loading rate used in the mechanical tests was far from the physiological one associated to fractures. While stepwise loading has been shown to properly evaluate the mechanical failure of bone structure in cores of trabecular bone extracted from the whole organ [56], when applied to spine segments it involves a redistribution of the fluids in the intervertebral discs and metastasis, and consequently a redistribution of the stress/strain in the vertebra that can results in different failure mechanisms associated to the viscous behaviour of the soft tissues. However, the combination of stepwise loading, microCT imaging, and DVC is the only approach available to measure the internal deformation of complex heterogeneous biological tissues, and approaches based on faster monotonic testing are not fully developed [31]. Furthermore, quasi-static loading has been hypothesised as a possible mechanism of vertebral failure [67]. Finally, the type of metastasis was assessed from qCT, as in the clinical practice, and double checked with the high-resolution microCT scans. Histology to confirm the type of lesion was not possible since the specimens were not fixed and stored frozen before testing. In fact fixation was found to affect the biomechanical properties of vertebrae and intervertebral discs [68].

5. Conclusions

In this work we have studied for the first time the volumetric deformation of vertebral bodies with different types of lesions. Vertebrae with lytic and mixed lesions showed the largest deformations and high likelihood of fracture. Blastic metastasis can lead to failure of the affected vertebra or of the adjacent healthy vertebra. This work showed that in most cases metastatic vertebral bodies fail similarly to those without lesions, with direct involvement of the endplates or of the tissue close to them. This approach, extended in the future to a larger number of spine segments and more complex loading conditions, can be used to identify the parameters of the lesion (e.g. type, size, location) that are most likely to induce failure of the vertebral body and that could inform new scoring systems, to validate computational models for predicting the vertebral strength and its risk of fracture, and to develop specific treatment for those vertebrae at high risk of fracture.

Declaration of competing interest

Data availability

Data will be made available on request.

Acknowledgements

Appendix A. Supplementary data

Supplementary data to this article can be found online at https://doi.org/10.1016/j.bone.2023.116814.

References

[1] R.L. Siegel, K.D. Miller, A. Jemal, Cancer statistics, 2020, CA A Cancer J. Clin. 70 (2020) 7–30, https://doi.org/10.3322/caac.21590.

[2] C. Ryan, K.C. Stoltzfus, S. Horn, H. Chen, A.V. Louie, E.J. Lehrer, D.M. Trifiletti, E. J. Fox, J.A. Abraham, N.G. Zaorsky, Epidemiology of bone metastases, Bone (2020) 115783, https://doi.org/10.1016/j.bone.2020.115783.

[3] A. Nazarian, D. von Stechow, D. Zurakowski, R. Müller, B.D. Snyder, Bone volume fraction explains the variation in strength and stiffness of cancellous bone affected by metastatic cancer and osteoporosis, Calcif. Tissue Int. 83 (2008) 368–379, https://doi.org/10.1007/s00223-008-9174-x.

[4] D. Roodman, Mechanisms of bone metastasis, N. Engl. J. Med. 10 (2004).

[5] C.M. Whyne, Biomechanics of metastatic disease in the vertebral column, Neurol. Res. 36 (2014) 493–501, https://doi.org/10.1179/1743132814Y.0000000362.

[6] L.E. Lanyon, Functional strain in bone tissue as an objective and controlling stimulus for adaptive bone remodelling, J. Biomech. 20 (1987) 1093–1098.

[7] P.J. Ehrlich, L.E. Lanyon, Mechanical strain and bone cell function: a review, Osteoporos. Int. 13 (2002) 688–700, https://doi.org/10.1007/s001980200095.

[8] C.B. Confavreux, H. Follet, D. Mitton, J.B. Pialat, P. Clézardin, Fracture risk evaluation of bone metastases: a burning issue, Cancers. 13 (2021) 5711, https://doi.org/10.3390/cancers13225711.

[9] C.G. Fisher, C.P. DiPaola, T.C. Ryken, M.H. Bilsky, C.I. Shaffrey, S.H. Berven, J. S. Harrop, M.G. Fehlings, S. Boriani, D. Chou, M.H. Schmidt, D.W. Polly, R. Biagini, S. Burch, M.B. Dekutoski, A. Ganju, P.C. Gerszten, Z.L. Gokaslan, M.W. Groff, N. J. Liebsch, E. Mendel, S.H. Okuno, S. Patel, L.D. Rhines, P.S. Rose, D.M. Sciubba, N. Sundaresan, K. Tomita, P.P. Varga, L.R. Vialle, F.D. Vrionis, Y. Yamada, D. R. Fourney, A novel classification system for spinal instability in neoplastic disease:

an evidence-based approach and expert consensus from the spine oncology study group, Spine 35 (2010) E1221–E1229, https://doi.org/10.1097/BRS.0b013e3181e16ae2.

[10] K.M. Whealan, S.D. Kwak, J.R. Tedrow, K. Inoue, B.D. Snyder, Noninvasive imaging predicts failure load of the spine with simulated osteolytic defects, J. Bone Joint Surg. (Am. Vol.) 82 (2000) 1240–1251, https://doi.org/10.2106/00004623-200009000-00004.

[11] L. Bollen, K. Groenen, W. Pondaag, C.S.P. van Rijswijk, M. Fiocco, Y.M. Van der Linden, S.P.D. Dijkstra, Clinical evaluation of the spinal instability neoplastic score in patients treated with radiotherapy for symptomatic spinal bone metastases, Spine. 42 (2017) E956–E962, https://doi.org/10.1097/BRS.0000000000002058.

[12] B.D. Snyder, M.A. Cordio, A. Nazarian, S.D. Kwak, D.J. Chang, V. Entezari, D. Zurakowski, L.M. Parker, Noninvasive prediction of fracture risk in patients with metastatic cancer to the spine, Clin. Cancer Res. 15 (2009) 7676–7683, https://doi.org/10.1158/1078-0432.CCR-09-0420.

[13] M. Palanca, G. Barbanti-Bròdano, D. Marras, M. Marciante, M. Serra, A. Gasbarrini, E. Dall'Ara, L. Cristofolini, Type, size and position of the metastatic lesions explain the deformation of the vertebrae under complex loading conditions, Bone 151 (2021) 1–11.

[14] M.A. Stadelmann, D.E. Schenk, G. Maquer, C. Lenherr, F.M. Buck, D.D. Bosshardt, S. Hoppe, N. Theumann, R.N. Alkalay, P.K. Zysset, Conventional finite element models estimate the strength of metastatic human vertebrae despite alterations of the bone's tissue and structure, Bone. 141 (2020), 115598, https://doi.org/10.1016/j.bone.2020.115598.

[15] D.E. Anderson, M.W. Groff, T.F. Flood, B.T. Allaire, R.B. Davis, M.A. Stadelmann, P.K. Zysset, R.N. Alkalay, Evaluation of load-to-strength ratios in metastatic vertebrae and comparison with age- and sex-matched healthy individuals, Front. Bioeng. Biotechnol. 10 (2022), 866970, https://doi.org/10.3389/fbioe.2022.866970.

[16] J.A. Kanis, Bone and cancer: pathophysiology and treatment of metastases, Bone. 17 (1995) S101–S105, https://doi.org/10.1016/8756-3282(95)00194-I.

[17] S. Bailey, M.A. Stadelmann, P.K. Zysset, D. Vashishth, R.N. Alkalay, Influence of metastatic bone lesion type and tumor origin on human vertebral bone architecture, matrix quality, and mechanical properties, J. Bone Miner. Res. (2022) jbmr.4539, https://doi.org/10.1002/jbmr.4539.

[18] F. Galbusera, Z. Qian, G. Casaroli, T. Bassani, F. Costa, B. Schlager, H.-J. Wilke, The role of the size and location of the tumors and of the vertebral anatomy in determining the structural stability of the metastatically involved spine: a finite element study, Transl. Oncol. 11 (2018) 639–646, https://doi.org/10.1016/j.tranon.2018.03.002.

[19] M.C. Costa, L.B.B. Campello, M. Ryan, J. Rochester, M. Viceconti, E. Dall'Ara, Effect of size and location of simulated lytic lesions on the structural properties of human vertebral bodies, a micro-finite element study, Bone Reports 12 (2020), 100257, https://doi.org/10.1016/j.bonr.2020.100257.

[20] G. Barbanti-Bròdano, M. Cappuccio, A. Gasbarrini, S. Bandiera, F.D. Salvo, F. Cosco, S. Boriani, Vertebroplasty in the treatment of vertebrae metastases: clinical cases and review of the literature, Eur. Rev. Med. Pharmacol. Sci. 11 (2007) 91–100.

[21] R.N. Alkalay, Effet of the metastatic defect on the structural responde and failure process of human vertebrae: an experimental study, Clin. Biomech. 30 (2015) 121–128.

[22] M. Palanca, G. Barbanti-Bròdano, L. Cristofolini, The size of simulated lytic metastases affects the strain distribution on the anterior surface of the vertebra, J. Biomech. Eng. 140 (2018) 111005, https://doi.org/10.1115/1.4040587.

[23] A. Rezaei, M. Tilton, H. Giambini, Y. Li, A. Hooke, A. Miller, L. Yaszemski, L. Lu, Three-dimensional surface strain analyses of simulated defect and augmented spine segments: a biomechanical cadaveric study, J. Mech. Behav. Biomed. Mater. 119 (2021), 104559.

[24] C.M. Whyne, S.S. Hu, J.C. Lotz, Burst fracture in the metastatically involved spine: development, validation, and parametric analysis of a three-dimensional poroelastic finite-element model, Spine. 28 (2003) 652–660, https://doi.org/10.1097/01.BRS.0000051910.97211.BA.

[25] C.E. Tschirhart, J.A. Finkelstein, C.M. Whyne, Metastatic burst fracture risk assessment based on complex loading of the thoracic spine, Ann. Biomed. Eng. 34 (2006) 494–505, https://doi.org/10.1007/s10439-005-9063-7.

[26] T.M. Jackman, A.I. Hussein, C. Curtiss, P.M. Fein, A. Camp, L. De Barros, E. F. Morgan, Quantitative, 3D visualization of the initiation and progression of vertebral fractures under compression and anterior flexion: visualization of initiation and progression of vertebral fracture, J. Bone Miner. Res. 31 (2016) 777–788, https://doi.org/10.1002/jbmr.2749.

[27] T.M. Jackman, A.M. DelMonaco, E.F. Morgan, Accuracy of finite element analyses of CT scans in predictions of vertebral failure patterns under axial compression and anterior flexion, J. Biomech. 49 (2016) 267–275, https://doi.org/10.1016/j.jbiomech.2015.12.004.

[28] M. McKay, T.M. Jackman, A.I. Hussein, A. Guermazi, J. Liu, E.F. Morgan, Association of vertebral endplate microstructure with bone strength in men and women, Bone 131 (2020) 115147. https://doi.org/10.1016/j.bone.2019.115147.

[29] A.J. Fields, G.L. Lee, T.M. Keaveny, Mechanisms of initial endplate failure in the human vertebral body, J. Biomech. 43 (2010) 3126–3131, https://doi.org/10.1016/j.jbiomech.2010.08.002.

[30] A. Sahgal, E.G. Atenafu, S. Chao, A. Al-Omair, N. Boehling, E.H. Balagamwala, M. Cunha, I. Thibault, L. Angelov, P. Brown, J. Suh, L.D. Rhines, M.G. Fehlings, E. Chang, Vertebral compression fracture after spine stereotactic body radiotherapy: a multi-institutional analysis with a focus on radiation dose and the spinal instability

neoplastic score, JCO 31 (2013) 3426–3431. https://doi.org/https://doi.org/10.1200/JCO.2013.50.1411.

[31] E. Dall'Ara, G. Tozzi, Digital volume correlation for the characterization of musculoskeletal tissues: current challenges and future developments, Front. Bioeng. Biotechnol. 10 (2022) 1010056, https://doi.org/10.3389/fbioe.2022.1010056.

[32] M. Palanca, G. De Donno, E. Dall'Ara, A novel approach to evaluate the effects of artificial bone focal lesion on the three-dimensional strain distributions within the vertebral body, PLoS ONE 16 (2021), e0251873, https://doi.org/10.1371/journal.pone.0251873.

[33] H.S. Hosseini, A.L. Clouthier, P.K. Zysset, Experimental validation of finite element analysis of human vertebral collapse under large compressive strains, J. Biomech. Eng. 136 (2014), 041006, https://doi.org/10.1115/1.4026409.

[34] A.I. Hussein, P.E. Barbone, E.F. Morgan, Digital volume correlation for study of the mechanics of whole bones, Procedia IUTAM 4 (2012) 116–125, https://doi.org/10.1016/j.piutam.2012.05.013.

[35] G.J. Kazakia, A.J. Burghardt, S. Cheung, S. Majumdar, Assessment of bone tissue mineralization by conventional x-ray microcomputed tomography: comparison with synchrotron radiation microcomputed tomography and ash measurements: assessment of bone tissue mineralization by microcomputed tomography, Med. Phys. 35 (2008) 3170–3179, https://doi.org/10.1118/1.2924210.

[36] E. Dall'Ara, D. Barber, M. Viceconti, About the inevitable compromise between spatial resolution and accuracy of strain measurement for bone tissue: a 3D zero-strain study, J. Biomech. 47 (2014) 2956–2963, https://doi.org/10.1016/j.jbiomech.2014.07.019.

[37] M. Palanca, L. Cristofolini, E. Dall'Ara, M. Curto, F. Innocente, V. Danesi, G. Tozzi, Digital volume correlation can be used to estimate local strains in natural and augmented vertebrae: an organ-level study, J. Biomech. 49 (2016) 3882–3890, https://doi.org/10.1016/j.jbiomech.2016.10.018.

[38] E. Dall'Ara, M. Peña-Fernández, M. Palanca, M. Giorgi, L. Cristofolini, G. Tozzi, Precision of digital volume correlation approaches for strain analysis in bone imaged with micro-computed tomography at different dimensional levels, Front. Mater. 4 (2017) 31, https://doi.org/10.3389/fmats.2017.00031.

[39] D.M.D. Abràmoff, Image processing with ImageJ, Biophoton. Int. 11 (2004) 36–42.

[40] D. Barber, D. Hose, Automatic segmentation of medical images using image registration: diagnostic and simulation applications, J. Medical Eng. Technol. 29 (2005) 53–63, https://doi.org/10.1080/03091900412331289889.

[41] D.C. Barber, E. Oubel, A.F. Frangi, D.R. Hose, Efficient computational fluid dynamics mesh generation by image registration, Med. Image Anal. 11 (2007) 648–662, https://doi.org/10.1016/j.media.2007.06.011.

[42] P.K. Sahoo, S. Soltani, A.K.C. Wong, A survey of thresholding techniques, Comput. Vis. Graph. Image Process. 41 (1988) 233–260, https://doi.org/10.1016/0734-189X(88)90022-9.

[43] M.L. Bouxsein, S.K. Boyd, B.A. Christiansen, R.E. Guldberg, K.J. Jepsen, R. Müller, Guidelines for assessment of bone microstructure in rodents using micro-computed tomography, J. Bone Miner. Res. 25 (2010) 1468–1486, https://doi.org/10.1002/jbmr.141.

[44] M. Stauber, R. Müller, Micro-computed tomography: A method for the non-destructive evaluation of the three-dimensional structure of biological specimens, in: J.J. Westendorf (Ed.), Osteoporosis, Humana Press, Totowa, NJ, 2008, pp. 273–292, https://doi.org/10.1007/978-1-59745-104-8_19.

[45] E. Dall'Ara, P. Varga, D. Pahr, P. Zysset, A calibration methodology of QCT BMD for human vertebral body with registered micro-CT images: calibration of QCT BMD with registered micro-CT images, Med. Phys. 38 (2011) 2602–2608. https://doi.org/https://doi.org/10.1118/1.3582946.

[46] G. Cavazzoni, L. Cristofolini, E. Dall'Ara, M. Palanca, Bone metastases do not affect the measurement uncertainties of a global digital volume correlation algorithm, Front. Bioeng. Biotechnol. 11 (2023), https://doi.org/10.3389/fbioe.2023.1152358.

[47] S. Rühling, A. Scharr, N. Sollmann, M. Wostrack, M.T. Löffler, B. Menze, A. Sekuboyina, M. El Husseini, R. Braren, C. Zimmer, J.S. Kirschke, Proposed diagnostic volumetric bone mineral density thresholds for osteoporosis and osteopenia at the cervicothoracic spine in correlation to the lumbar spine, Eur. Radiol. 32 (2022) 6207–6214, https://doi.org/10.1007/s00330-022-08721-7.

[48] The American College of Radiology, Acr–Spr–Ssr Practice Parameter for the Performance of Musculoskeletal Quantitative Computed Tomography (Qct), 2018.

[49] T. Fujiwara, K. Akeda, J. Yamada, T. Kondo, A. Sudo, Endplate and intervertebral disc injuries in acute and single level osteoporotic vertebral fractures: is there any association with the process of bone healing? BMC Musculoskelet. Disord. 20 (2019) 336, https://doi.org/10.1186/s12891-019-2719-5.

[50] E. Oh, H. Kim, J.W. Kwon, Y.C. Yoon, H.S. Kim, Differentiation between spinal subchondral bone metastasis with focal pathologic endplate fracture and oedematous Schmorl's node, J. Med. Imaging Radiat. Oncol. (2021), https://doi.org/10.1111/1754-9485.13365.

[51] R.L. Ferguson, B.L. Allen, A mechanistic classification of thoracolumbar spine fractures, Clin. Orthop. Relat. Res. 189 (1984) 77???88, https://doi.org/10.1097/00003086-198410000-00009.

[52] S.K. Eswaran, A. Gupta, M.F. Adams, T.M. Keaveny, Cortical and trabecular load sharing in the human vertebral body, J. Bone Miner. Res. 21 (2005) 307–314, https://doi.org/10.1359/jbmr.2006.21.2.307.

[53] A. Nazarian, M. Stauber, D. Zurakowski, B.D. Snyder, R. Müller, The interaction of microstructure and volume fraction in predicting failure in cancellous bone, Bone. 39 (2006) 1196–1202, https://doi.org/10.1016/j.bone.2006.06.013.

[54] D. Marras, M. Palanca, L. Cristofolini, Effects induced by osteophytes on the strain distribution in the vertebral body under different loading configurations, Front.

Bioeng. Biotechnol. 9 (2021), 756609, https://doi.org/10.3389/fbioe.2021.756609.

[55] R.E. Coleman, P.I. Croucher, A.R. Padhani, P. Clézardin, E. Chow, M. Fallon, T. Guise, S. Colangeli, R. Capanna, L. Costa, Bone metastases, Nat. Rev. Dis. Prim. 6 (2020) 83, https://doi.org/10.1038/s41572-020-00216-3.

[56] A. Nazarian, R. Müller, Time-lapsed microstructural imaging of bone failure behavior, J. Biomech. 37 (2004) 55–65, https://doi.org/10.1016/S0021-9290(03)00254-9.

[57] H. Yang, M.G. Jekir, M.W. Davis, T.M. Keaveny, Effective modulus of the human intervertebral disc and its effect on vertebral bone stress, J. Biomech. 49 (2016) 1134–1140, https://doi.org/10.1016/j.jbiomech.2016.02.045.

[58] C.E. Tschirhart, A. Nagpurkar, C.M. Whyne, Effects of tumor location, shape and surface serration on burst fracture risk in the metastatic spine, J. Biomech. 37 (2004) 653–660, https://doi.org/10.1016/j.jbiomech.2003.09.027.

[59] L. Cristofolini, In vitro evidence of the structural optimization of the human skeletal bones, J. Biomech. 48 (2015) 787–796, https://doi.org/10.1016/j.jbiomech.2014.12.010.

[60] L. Cristofolini, N. Brandolini, V. Danesi, M.M. Juszczyk, P. Erani, M. Viceconti, Strain distribution in the lumbar vertebrae under different loading configurations, Spine J. 13 (2013) 1281–1292, https://doi.org/10.1016/j.spinee.2013.06.014.

[61] V. Danesi, G. Tozzi, L. Cristofolini, Application of digital volume correlation to study the efficacy of prophylactic vertebral augmentation, Clin. Biomech. 39 (2016) 14–24, https://doi.org/10.1016/j.clinbiomech.2016.07.010.

[62] U. Berlemann, S.J. Ferguson, Adjacent vertebral failure after vertebroplasty, J. Bone Joint Surg. 84 (2002) 5.

[63] M.C. Costa, P. Eltes, A. Lazary, P.P. Varga, M. Viceconti, E. Dall'Ara, Biomechanical assessment of vertebrae with lytic metastases with subject-specific finite element models, J. Mech. Behav. Biomed. Mater. 98 (2019) 268–290, https://doi.org/10.1016/j.jmbbm.2019.06.027.

[64] J. Widmer, F. Cornaz, G. Scheibler, J.M. Spirig, J.G. Snedeker, M. Farshad, Biomechanical contribution of spinal structures to stability of the lumbar spine—novel biomechanical insights, Spine J. 20 (2020) 1705–1716, https://doi.org/10.1016/j.spinee.2020.05.541.

[65] A. Shirazi-Adl, G. Drouin, Load-bearing role of facets in a lumbar segment under sagittal plane loadings, J. Biomech. 20 (1987) 601–613.

[66] International Osteoporosis Foundation Fracture Working Group, W.F. Lems, J. Paccou, J. Zhang, N.R. Fuggle, M. Chandran, N.C. Harvey, C. Cooper, K. Javaid, S. Ferrari, K.E. Akesson, Vertebral fracture: epidemiology, impact and use of DXA vertebral fracture assessment in fracture liaison services, Osteoporos. Int. 32 (2021) 399–411, https://doi.org/10.1007/s00198-020-05804-3.

[67] T.S. Keller, D.E. Harrison, C.J. Colloca, D.D. Harrison, T.J. Janik, Prediction of osteoporotic spinal deformity, Spine 28 (2003) 455–462, https://doi.org/10.1097/01.BRS.0000048651.92777.30.

[68] H.-J. Wilke, S. Krischak, L.E. Claes, Formalin fixation strongly influences biomechanical properties of the spine, J. Biomech. 29 (1996) 1629–1631.